

Physical Conditions in the Inner Narrow-Line Region of the Seyfert 2 Galaxy NGC 1068¹

Steven B. Kraemer^{2,3}, José R. Ruiz², & D. Michael Crenshaw²

Received 1998 February 18; accepted 1998 May 16

To appear in *The Astrophysical Journal*

arXiv:astro-ph/9806339v1 25 Jun 1998

¹Based on observations made with the NASA/ESA Hubble Space Telescope, obtained from the data archive at the Space Telescope Science Institute. STScI is operated by the Association of Universities for Research in Astronomy, Inc. under the NASA contract NAS5-26555.

²Catholic University of America, NASA/Goddard Space Flight Center, Code 681, Greenbelt, MD 20771.

³Email: stiskraemer@yancey.gsfc.nasa.gov.

ABSTRACT

The physical conditions in the inner narrow line region (NLR) of the Seyfert 2 galaxy, NGC 1068, are examined using ultraviolet and optical spectra and photoionization models. The spectra are *Hubble Space Telescope* (*HST*) archive data obtained with the Faint Object Spectrograph (FOS). We selected spectra of four regions, taken through the $0''.3$ FOS aperture, covering the full FOS 1200 Å to 6800 Å waveband. Each region is approximately 20 pc in extent, and all are within 100 pc of the apparent nucleus of NGC 1068. The spectra show similar emission-line ratios from wide range of ionization states for the most abundant elements. After extensive photoionization modeling, we interpret this result as an indication that each region includes a range of gas densities, which we included in the models as separate components. Supersolar abundances were required for several elements to fit the observed emission line ratios. Dust was included in the models but apparently dust to gas fraction varies within these regions. The low ionization lines in these spectra can be best explained as arising in gas that is partially shielded from the ionizing continuum.

Although the predicted line ratios from the photoionization models provide a good fit to the observed ratios, it is apparent that the model predictions of electron temperatures in the ionized gas are too low. We interpret this as an indication of additional collisional heating due to shocks and/or energetic particles associated with the radio jet that traverses the NLR of NGC 1068. The density structure within each region may also be the result of compression by the jet.

Subject headings: galaxies: individual (NGC 1068) – galaxies: Seyfert

1. Introduction

NGC 1068, one of the initial set of emission line galaxies studied by Seyfert (1943), is the nearest ($z=0.0036$) and the best studied of the Seyfert 2 galaxies. NGC 1068 has been observed extensively in all wavebands from the radio to the X-ray. Not only is there evidence of ionizing radiation from the central AGN, but a prominent radio jet exists in the NLR (Wilson & Ulvestad 1983), and there is a starburst ring approximately 1 kiloparsec from the nucleus (Snijders, Briggs, & Boksenberg 1982, Bruhweiler, Troung, & Altner 1991). The detection of polarized optical continuum and broad permitted lines (Miller & Antonucci 1983, Antonucci & Miller 1985) in the nucleus of NGC 1068 was the inspiration for the "unified model" for Seyfert galaxies, in which the differences between types 1 and 2 were attributed to viewing angle (Antonucci 1994), with Seyfert 2's characterized by obscuration of their central engines.

Due to its relative proximity, NGC 1068 offers unique opportunity to study the detailed physics of the NLR gas. Studies of the conditions in the NLR can provide a check on the estimates of the luminosity and spectral characteristics of the intrinsic ionizing continuum proposed by Pier et al. (1994) and Miller, Goodrich, & Mathews (1991). Ground based observations and analysis of the extended narrow line region (Balick & Heckman 1985, Evans & Dopita 1986, Bergeron, Petitjean, & Durret 1989) have shown that gas at large distances from the nucleus (\sim kiloparsecs) is likely to be photoionized by the radiation from the central active galactic nucleus (AGN). It follows that photoionization must be an important if not dominant process in the inner NLR of NGC 1068 as well. Before *HST*, it was difficult to examine the conditions in the inner 100 pc. Ground based optical spectra (cf. Koski 1978) and UV spectra from *IUE* (Snijders et al. 1982) that sampled large areas ($\geq 3''$) within NGC 1068 did not have the resolution to provide the necessary constraints on models of the emission line gas. With *HST* resolution and spectral coverage, we now

have access to spatially-resolved spectra of the inner NLR.

Although it is clear that the NLR gas is photoionized (Netzer 1997), it is possible that collisional processes are important as well (Kriss et al. 1992). Detailed photoionization models can help distinguish between the contributions of various possible sources of ionization and heating in the NLR. A better determination of the relative contributions of such process may lead to an understanding of the physical nature of the NLR, and possibly its origin and evolution. Even though the ionizing continuum in NGC 1068 cannot be directly observed, the relative radial distances and physical extents of the regions observed are known, important new constraints on the models.

2. Observations and Analysis

There are a large number of FOS observations of NGC 1068 in the *HST* archives. FOS spectra were obtained of the brightest point in the visible region, which we refer to as the “nucleus”; some of the spectra have been published by Caganoff et al. (1991) and Antonucci et al. (1994). Spectra were also obtained at various offset positions from the nucleus, but have not been published. In the *HST* archives, these positions are often referred to as “clouds” (e.g., “Cloud 1”), but we will refer to them as “positions” (e.g., “Position 1”), since FOC and WFPC2 [O III] images show that even the FOS 0".3 aperture encompasses a number of emission-line knots. We chose to limit the number of spectra for this study to satisfy several criteria. First, the position observed must have full wavelength coverage from 1200 – 6800 Å at good resolution ($\lambda/\Delta\lambda \approx 1000$), to provide a full range of emission-line diagnostics; thus only pointings that include observations with the G130H, G190H, G270H, G400H, and G570H gratings were used. Second, we wanted to concentrate on regions of small spatial extent, to minimize the range in physical conditions, so only observations through the 0".3 aperture were included. Finally, for observations obtained of

the same region at different times, the acquisition techniques had to be the same, and we required that the spectra match well where they overlap. Table 1 gives a summary of the observations that we used. Note that observations of “NGC1068” and “NGC1068-NUC” are of the same region (the “nucleus”).

Our requirements resulted in UV and optical spectra of the nucleus and three offset positions in the inner NLR through a $0''.3$ aperture. The nucleus was acquired by peakups through successively smaller apertures ($1''.0$, $0''.5$, and $0''.3$) using light from the G270H grating. Spectra of the other positions were obtained by offsetting to positions of bright emission seen in the original WF/PC narrow-band images (centered on various emission lines such as [O III]). Peakups and spectra were obtained with the FOS/BLUE detector and G130H and G190H gratings, and with the FOS/RED detector and G270H, G400H, and G570H gratings. In addition, blue G270H spectra were obtained of the nucleus after peakups with the blue detector. In this case, after scaling the red G270H spectrum by a factor of 1.1, the features in both blue and red G270H spectra are essentially identical. Thus, we are confident that peakups on the nucleus performed at different times and with different detectors resulted in observations of the same region. Since the offsets are highly accurate, and the spectra at each offset position matched to within 10% in the wavelength regions of overlap, we are confident of these pointings as well. To account for the small ($\leq 10\%$) absolute flux differences, all of the spectra from a given position were scaled to match the flux level of the red G270H spectra.

Figure 1 shows the locations of the aperture for these pointings, superimposed on an FOC [O III] $\lambda 5007$ image obtained from the *HST* archives and the axis of the radio jet (Gallimore et al. 1996). We note that the FOS observations were obtained prior to the installation of COSTAR on *HST* in 1993 December, so that a substantial amount of light from outside the projected aperture is included in each of these spectra. These effects are

discussed in greater detail below. At the distance of NGC 1068, $0''.3$ corresponds to 21 pc (for $z=0.0036$ and $H_0 = 75 \text{ km s}^{-1} \text{ Mpc}^{-1}$).

Figure 2, 3, and 4 show the far-UV, near-UV, and optical spectra for each position. We note that the N V $\lambda\lambda 1239, 1243$ and C IV $\lambda\lambda 1548, 1551$ doublets, normally blended together in Seyfert 2 spectra, are resolved in some of the far-UV spectra, since we are isolating specific kinematic regions and these lines are therefore relatively narrow. The blue component of the doublet *appears* to be smaller than the red component in each case, because Galactic and intrinsic absorption features (probably from the halo of NGC 1068) are absorbing the blue side of the doublet emission in each case. We also note that the spectra from different positions are very similar in appearance, given the differences in absolute fluxes, and that the N V and [Ne V] $\lambda\lambda 3346, 3424$ lines are unusually strong in each spectrum. We will explore these issues later in the paper.

We measured the fluxes of most of the narrow emission lines by direct integration over a local baseline determined by linear interpolation between adjacent continuum regions. For severely blended lines such as H α and [N II] $\lambda\lambda 6548, 6584$, we used the [O III] $\lambda 5007$ profile as a template to deblend the lines (see Crenshaw & Peterson 1986). We then determined the reddening of the narrow emission lines from the observed He II $\lambda 1640/\lambda 4686$ ratio, the Galactic reddening curve of Savage & Mathis (1979), and an intrinsic He II ratio of 7.2, which is expected from recombination (Seaton 1978) at the temperatures and densities typical of the NLR (see also Section 3). We determined errors in the dereddened ratios from the sum in quadrature of the errors from three sources: photon noise, different reasonable continuum placements, and reddening.

Table 2 gives the dereddened narrow-line ratios, relative to H β , and errors in the dereddened ratios for each position. Inspection of this table shows that the emission-line ratios from the different regions are indeed very similar. At the end of the table, we give

the $H\beta$ fluxes ($\text{ergs s}^{-1} \text{ cm}^{-2}$) in the aperture and the reddening values that we determined from the He II ratios.

As we mentioned earlier, these observations were obtained prior to the installation of COSTAR. Hence, the presence of broad wings on the point-spread function at the aperture plane leads to substantial contamination of the observed flux by emission-line knots outside of the projected aperture. To estimate this effect on the observed spectra, we retrieved (from the STScI) a model pre-COSTAR point spread function (PSF) for the FOS red detector at 5000 \AA , which was generated and described by Evans (1993). We interpolated over the reseaux in the post-COSTAR FOC [O III] image in Figure 1 (which has a spatial resolution of $0''.014$ per pixel), extracted subimages through apertures of different sizes, and convolved the original image and subimages with the FOS PSF image. We then determined the percentage of the [O III] flux in the spectrum of each region that is contributed by emission within the projected $0''.3$ aperture, within a concentric aperture of diameter $0''.6$, and from the remainder of the NLR flux in the FOC image. These values are respectively 61%, 22%, and 17% for the nucleus; 53%, 30%, and 17% for position 1; 54%, 25%, and 21% for position 2; and 65%, 20% and 15% for position 3. Thus, in these cases, we are sampling regions considerably larger than the projected aperture sizes; however, in each pointing, at least $\sim 80\%$ of the [O III] flux is coming from within $\sim 0''.6$ of the aperture centers. Position 1 is $\sim 0''.2$ from the “nucleus”, so we are primarily sampling the same region in this case. For positions 2 and 3, we are sampling regions that are relatively distinct, since they are $0''.6$ and $1''.5$ from the nucleus.

3. Photoionization Models

As in our previous studies (e.g., Kraemer et al. 1998), we have taken a simple approach in setting the initial input values for photoionization models. In previous cases where we

could not resolve the emission-line region, we could effectively adjust the distance of the emission-line gas from the source of the ionizing radiation to obtain a good match with the observations. With the current data set we have spectra from spatially resolved regions and, therefore, the distance of the gas from the ionizing source is more tightly constrained. In turn, we can be more flexible in adjusting input parameters such as abundances and optical thickness, if our initial parameters are not sufficient. Such an approach can produce a better fit to the observed line ratios, but it is important to bear in mind that it still might not result in a unique solution for the set of physical conditions in the emission line region. We will return to this point in the following section.

The photoionization code used for this study has been described in detail in our previous papers (cf. Kraemer et al. 1998), and we will not repeat the description here. A few points should be mentioned, however. First, it is important to bear in mind that this code assumes a slab geometry, with photon escape out the illuminated face. The effects of dust are included, including internal reddening, trapping of UV resonance lines and screening of the ionization radiation. Forward scattering by the grains is assumed. For a full explanation of the treatment of dust in this code, see Kraemer (1985). As per the standard convention, models are parameterized in terms of the density of atomic hydrogen (N_H) and the dimensionless ionization parameter at the illuminated face of the cloud:

$$U = \int_{\nu_0}^{\infty} \frac{L_{\nu}}{h\nu} d\nu / 4\pi D^2 N_H c, \quad (1)$$

where L_{ν} is the frequency dependent luminosity of the ionizing continuum, D is the distance between the cloud and the ionizing source and $h\nu = 13.6$ eV.

4. Choosing the Model Input Parameters

In spite of the pre-COSTAR PSF problems described in section 2, we know that the majority of the line emission seen in these spectra arise in or near the projected aperture locations shown in Figure 1. The spectra from each of these regions show a wide range of ionization states for the most abundant elements, indicating gas with a range of physical conditions within each region. In simple multi-component models of an entire NLR (see Kraemer et al. 1994), one can include contributions from gas in various ionization states by placing the components at different distances from the ionizing source. This means that there can be a large amount of low-ionization, low density gas at large radial distances; having a large volume of this gas can balance the fact that such components have low emissivity relative to higher ionization denser material close to the ionizing source, as long as the covering factor of the inner component is small. We do not have this flexibility in modeling these spectra. If the line emission is from photoionized gas, there must be a range in density within the observed regions. After running an initial set of simple multicomponent models, it became clear that we needed additional parameters to match the observations. These parameters include elemental abundances, "shielding" of one of our components, optical depth, and dust.

Although previous photoionization studies have suggested that the elemental abundances in the NLR may be non-solar (Osterbrock 1989), line ratios indicative of non-solar abundances can often be explained by including multi-component models of varying density. For these data, however, there are clear indications of non-solar abundances. For example, as discussed by Netzer (1997), the ratio of the O III] λ 1664/ N III] λ 1750 lines can be used to estimate the ratio of elemental oxygen to nitrogen, since their ionization regions tend to show large overlap. The theoretical ratio is as follows:

$$\frac{I(\lambda 1664)}{I(\lambda 1750)} = 0.41 T_4^{-0.04} \exp(-0.43/T_4) \frac{N(O^+)}{N(N^+)} \quad (2)$$

where T_4 is the temperature in units of 10,000K. The average intensity ratio from the four regions sampled is 0.65. If we assume $T=15,000\text{K}$, $N(O)/N(N)$ is ~ 2.1 , which is 0.36 times solar. Netzer interprets this as a large oxygen underabundance, and offers the observed $O\text{ III}] \lambda 1664/C\text{ III}] \lambda 1909$ ratio as further evidence, since it yields an $N(O)/N(C) \sim 0.73$. Averaging over the four regions, we obtain $N(O)/N(C) \sim 1.8$, which is approximately solar. Therefore, it is likely that we are seeing enhanced nitrogen, rather than depleted oxygen.

Another indication that the nitrogen is supersolar is the ratio of the $N\text{ V} \lambda 1240$ line to the $\text{He II} \lambda 1640$. In photoionized gas, the $N\text{ V}/\text{He II}$ ratio is typically less than unity (Ferland et al. 1996). Although this ratio can increase if the gas is so optically thin that the edge of the He^{++} Stromgren zone is never attained, in such cases the $O\text{ V} \lambda 1216$ and $O\text{ VI} \lambda 1035$ lines become inordinately strong (Netzer was able to achieve such ratios without excess $O\text{ V}$ and $O\text{ VI}$ emission by depleting oxygen by a factor of 3, which we do not think is supported by the observations). Ferland et al. suggest that relative enhancement of nitrogen can better explain such line ratios. Although their study was of the spectra of luminous QSOs, not only are the same physical processes at work in the ionized gas, it is not too surprising that there may be heavily reprocessed material in the nucleus of a Seyfert galaxy, since it is possible that the AGN phenomenon was preceded by a massive nuclear starburst (cf. Osterbrock 1993) Finally, the $[\text{N II}] \lambda\lambda 6548, 6584$ lines are quite strong in these spectra (4 to 5 times the strength of $H\beta$) while the $[\text{O II}] \lambda 3727$ line is weak. Although this is possibly due to collisional suppression of the $[\text{O II}]$ line, it is also plausible that we are seeing the effect of overabundance of nitrogen. This will be explained in more detail in the discussion of the model results. For the models, we assume a three-times solar

nitrogen abundance.

The lines of Ne^{+3} , Ne^{+4} and Fe^{+6} are quite strong in all these spectra. Fitting the coronal lines with solar abundances is often a problem for photoionization models (Kraemer et al. 1998), but as Oliva (1997) suggests, they can be enhanced if these elements are overabundant. Furthermore, from their analysis of *ASCA* data, Netzer & Turner (1997) postulate that the Fe/O ratio is quite high in the X-ray emitting gas in NGC 1068. For these models, we have assumed that both iron and neon are supersolar by a factor of 2 in abundance.

Although it is possible that other elements may be overabundant, there is no indication from the spectra that this is the case. Therefore, we have chosen to keep them at solar abundances. The numerical abundances, relative to hydrogen, assumed for these model are as follows: He=0.1, C= 3.4×10^{-4} , O= 6.8×10^{-4} , N= 3.6×10^{-4} , Ne= 2.2×10^{-4} , S= 1.5×10^{-5} , Si= 3.1×10^{-5} , Mg= 3.3×10^{-5} , Fe= 8.0×10^{-5} .

We have assumed in these simple models that the gas is photoionized by radiation from the central AGN. In NGC 1068, as in most Seyfert 2 galaxies, it is impossible to measure the intrinsic ionizing continuum directly, since the inner regions of these objects are usually obscured by a large column of dusty gas. The ionizing continuum is only observed by light scattered into our line of sight by a scattering medium, possibly consisting of free electrons (see Antonucci 1994 for the details of this basic model). There have been attempts (Miller et al. 1991, Pier et al. 1994) to determine the intrinsic luminosity and spectral energy distribution (SED) of NGC 1068 based on observations in the non-ionizing UV and X-ray, assumptions about the nature of the scattering medium, and comparison to AGN whose nuclei can be observed more directly. The results of these two papers are similar; we have chosen an SED similar to that assumed by Pier et al. as it is the simpler of the two. It consists of a broken power, $F_\nu = K\nu^{-\alpha}$, where:

$$\alpha = 1.6, 13.6eV \leq h\nu < 2000eV \quad (3)$$

$$\alpha = 0.5, h\nu \geq 2000eV \quad (4)$$

In addition, we have taken the observed fluxes at $\log(\nu) = 15.376$ and 17.684 quoted by the authors and assumed the same value for the fraction of intrinsic light reflected into our line of sight, $f_{rel}=0.015$. Integrating over frequency and dividing by f_{rel} yields a luminosity in ionizing photons of $4 \times 10^{54} \text{ sec}^{-1}$, which is typical of Seyfert 1 nuclei.

As mentioned above, the range of emission lines seen in the spectra of each of these regions indicate a mix of physical conditions. Although emission from a wide range of ionization states is possible from a single component characterized by one atomic density, the most highly ionized parts of such a region would have the highest emissivity (greatest electron density and temperature) and therefore would dominate the integrated spectrum. Since we see strong lines from both low and high ionization states, it is likely that the physical properties of the regions where these lines form are indeed different, and that we are seeing emission from distinct regions.

An initial guess at temperature and density can be derived from the ratio of [O III] $\lambda\lambda 5007, 4959$ / [O III] $\lambda 4363$ (Osterbrock 1974). Averaged over the four spectra, this ratio is ~ 46 , indicating a temperature in excess of 20,000K in the low density limit. It is difficult to obtain such a high electron temperature in the O^{++} zone in photoionized gas. It is possible that we are seeing a modest modification of this ratio by collisional effects. If we assume a density of $1 \times 10^5 \text{ cm}^{-3}$, the observed [O III] line ratio yields a temperature = 17,000K, which is more characteristic of the O^{++} in photoionized gas. Therefore, we assign this density to one component in these models. It is important, however, to note that this simple assumption may not be correct if mechanisms other than photoionization contribute to the thermal balance in the emission line gas, as we shall discuss in section 7.

The gas in which the bulk of the [N II] emission is formed must be characterized by a lower ionization parameter. There are three ways in which U can be lowered: increase D , increase N_H , or decrease L . Since the individual regions are small (~ 20 pc) and a few tens of parsecs away from the putative central source, there cannot be sufficient range in distance to account for this drop. Since the O^{++} region is best characterized by a density of 10^5cm^{-3} , increasing the density of the lower excitation gas would weaken the [N II] emission due to collisional de-excitation. The simplest explanation is that the low excitation gas must see a different ionizing continuum. Although one possibility is local sources of ionizing radiation (Axon et al. 1998), we propose an alternative. The low ionization (N^+) gas is screened from the central source by the O^{++} gas, it is therefore ionized by a filtered continuum. Gas of the same, or lower, density, will then be in a lower state of ionization. Ferland & Mushotzky (1982) proposed that the NLR of NGC 4151 is illuminated by radiation that is partly absorbed by the BLR gas (the so-called "leaky absorber" model). The leaky absorber SED is much harder than the intrinsic SED of the galaxy, and the conditions in the NLR gas are strongly influenced by the effects of X-ray ionization. Collisional excitation of $Ly\alpha$ and $H\alpha$ become important processes in such gas. Also, extended partially ionized zones can form. Evidence for both these effects can be seen in this set of spectra. The larger than Case B $H\alpha/H\beta$ ratio is most likely due to collisional enhancement of $H\alpha$. Also, if the emissivity of the gas in which the [NII] lines form is low compared to that in which the higher excitation lines form, there must be a large volume of it to produce low excitation lines of comparable strength. We found in generating these models, that placing gas of lower density behind the O^{++} region was more likely to produce extended zones of $N(H^+)/N(H) \approx 25\%$. At very low density the emissivity of the gas was so low that the emitting regions had to be much larger than the sizes of the regions observed. Note that, in this type of model, the covering factor of the low excitation gas must be the same as the high excitation gas, so the area of this component is constrained. We found that this component could be best modeled by

assuming a density of $5 \times 10^4 \text{cm}^{-3}$ and an input spectrum filtered through a column density of $\sim 2 \times 10^{21} \text{cm}^{-2}$.

Finally, there must be another component in which the highest excitation lines, in particular N V $\lambda 1240$, arise. For the sake of simplicity, we assigned the same density to this component as used for the low excitation gas ($5 \times 10^4 \text{cm}^{-3}$). Although this is arbitrary, it does produce a simple and self-consistent model. Specifically, there is a component of gas of density $5 \times 10^4 \text{cm}^{-3}$, which is partially shielded from the central source by a higher density component. The high density gas is relatively optically thick, but is physically thin ($\sim 10^{-2}$ parsecs). The covering factors of the high density component and the shielded gas are equal. The relative covering factors of the high density gas and the unshielded lower density gas may vary among the regions.

In each of the four spectra, the ratio $\text{Ly}\alpha/\text{H}\beta$ is less than 20. The low density ratio from recombination is 24. Therefore, it is likely that dust mixed in with the emission line gas is responsible for the destruction of the Lyman alpha photons. The strength of the other resonance lines, specifically N V $\lambda 1240$ and C IV $\lambda 1550$, indicate that there cannot be much dust in the most highly ionized gas. Furthermore, the presence of the Fe^{+6} and Mg^{+} lines infer that the depletion of these refractory elements into grains cannot be near total, as it is in the Galactic interstellar medium (Seab & Shull 1983). Therefore, we have assumed different dust fractions in each of the three components in this model, as suggested by Netzer (1997). The highest ionization gas is dust free. The low ionization gas has a fraction of graphite dust 30% that found in the galactic interstellar medium. The medium ionization component is quite dusty with dust fraction of graphite and silicate dust 75% and 50% the galactic value, respectively. The depletions of carbon, oxygen, silicon, magnesium, and iron are scaled by these dust fractions, assuming galactic interstellar medium values: 80% for carbon, 20% for oxygen and complete depletion for the refractory elements. The

dust fractions assumed are arbitrary, but the model results are not particularly sensitive to the exact fraction of the different types of dust. The main point for these models is that assuming a mix of dusty and dust-free gas yields the best fit to the observed line ratios.

5. Model Results

Our approach in modeling these regions in NGC 1068 was to fit the O^{++} emission gas first, and then add the low excitation component. This was, of course, necessitated by the fact that we have assumed the low excitation gas is ionized by a continuum filtered by the O^{++} component. Once these two models were complete, we added the third component, primarily to fit the N V $\lambda 1240$ line. Having arrived at the densities of these three components as described above, we set the ionization parameters for the models. In order to avoid adding additional components, we set the ionization parameter high enough for the O^{++} that there would be significant [Ne V] and [Fe VII] emission; specifically, $U = 10^{-1.3}$, which, given the derived luminosity in ionizing photons, sets the distance from the central source at 15 parsecs. The four pointings in this set of data span a region of ~ 70 parsec from the central source. Given the uncertainty in the actual location of the source and the value of the fraction of reflected continuum (Pier et al. 1994), the choice of distance is plausible and puts our model region right in the middle of the set of FOS pointings. At this distance, the high ionization component is characterized by an ionization parameter, $U = 10^{-1}$.

It is clear from the SED of the ionizing continuum and the observed He II $\lambda 4686/H\beta$ ratio that much of the gas in these regions is optically thin at the Lyman limit. For optically thick gas, a simple photon counting calculation (cf Kraemer et al. 1994) yields a $4686/H\beta$ ratio ~ 0.16 ; observed values range from 0.43 to 0.59. The presence of a large fraction of optically thin (matter bounded) gas would increase the relative strength of the highest

ionization lines in the composite spectrum, compared to the composite spectrum from a region composed entirely of optically thick (radiation bounded) gas. This is supported by the fact that the strongest relative [Ne V] $\lambda 3426$ emission is seen in the same region that has the strongest He II $\lambda 4686$. There is no definitive way to determine the exact optical (and physical) thickness of each component of emission line gas in these regions. We decided, a priori, to truncate the integration in the O^{++} component at an optical depth of 10 at the Lyman limit. The resulting filtered spectrum is shown in Figure 5, and shows complete absorption at the He II Lyman limit, and strong absorption at the hydrogen Lyman limit; the physical conditions in gas photoionized by this continuum will be strongly effected by X-ray ionization and heating processes, as noted above. The resulting ionization parameter for the shielded gas was $10^{-2.35}$, with most of the energy in X-rays. We truncated the integration for the shielded component when the ionized fraction of the gas dropped below 5% and there was no longer significant line emission generated other than [N I] $\lambda 5200$ and [O I] $\lambda\lambda 6300, 6364$, neither of which are strong in these data.

Since the relative contributions from the O^{++} and shielded components are linked, there is at least some basis for truncating the integration of the O^{++} at the chosen optical depth. Picking the point to truncate the integration of the high ionization component is somewhat more arbitrary. We chose to truncate the model when we reached an optical depth of 10 at the He II Lyman limit, although there are indications from the predicted line ratios this component might be even thinner.

The results of the three component models are given in Table 3, along with the composite spectrum line ratios and a dereddened "observed" spectrum, averaged over the four sets of observations. The relative contributions to the composite spectrum are as follows: 25% from the high ionization component, 50% from the O^{++} component and 25% from the shielded component. We can check the plausibility of these ratios by comparing

the total $H\beta$ emission from each component. We only know one dimension of these slabs: the physical depth from the ionized face to the point where we truncated the integration. Comparing the product of the physical depth and the average emissivity gives a measure of the possible contribution from each component. The ratio of this product for the O^{++} and high ionization component is ~ 2 , which implies comparable covering factors for each of these components and supports the ratio of relative contribution used for the composite spectrum. The ratio of the products from the O^{++} and shielded components is ~ 4 , or approximately twice the ratio used in the composite. Since these two components are restricted to the same covering factor, as described above, it would seem that we do not have enough of the shielded gas. One obvious explanation is that there is additional shielded gas 'behind' the high ionization component. There may be other explanations as well; we will address this in the following section.

Comparison of the composite line ratios with the averaged observed ratios in Table 3 shows good agreement for the majority of emission lines. In particular, these include the [Fe VII] lines, [Ne V] $\lambda 3426$, [Ne III] $\lambda 3869$, [N II] $\lambda\lambda 6584, 6584$ [O II] $\lambda 3727$, [S II] $\lambda\lambda 6716, 6731$, C IV $\lambda 1550$, and N V $\lambda 1240$. The fact that the model predictions are good for lines of such a wide range of ionization state indicates that our overall balance of high and low excitation gas is reasonable. Also, the model predictions support our assumptions about the elemental abundances, since relative strengths of the iron, neon and nitrogen lines would all decrease if solar abundances were assumed for these elements. The [O III] $\lambda 5007/\lambda 4363$ ratio is also in good agreement with the observations, but this was to be expected since the choice of density and ionization parameter for the O^{++} component was based on this ratio. The predicted ratio of the [O I] $\lambda 6300/([O I] \lambda 6364 + [Fe X] \lambda 6374)$ is also in agreement with the observations, showing that the 6364 line is indeed blended with [Fe X], although the strength of these lines relative to $H\beta$ is somewhat high. The predictions of the ratios of the He II lines to $H\beta$ are also in good agreement with the observations, which support our

inclusion of matter bounded gas in the composite model.

From the model predictions we can determine the size of the emitting regions and the total amount of excited gas, using the relative contributions given above and comparing them to total $H\beta$ emission from the nucleus. Assuming the distance to NGC1068 is 20 Mpc and a filling factor within the emitting region of unity we obtain a minimum volume of $\sim 1 \text{ pc}^3$; this is quite reasonable given the 20 parsec extent of each region their apparent clumpiness (see Figure 1). We compute an actual filling factor of $\sim 10^{-4}$. The total mass of gas required is $\sim 8,000 M_{\odot}$, which is not unreasonable within such a volume.

Although we were able to obtain a reasonable fit to the data with this model, we would not suggest that this is a unique but, rather, possible solution. In addition to the problem of emissivity and covering factor of the shielded component, there are several discrepant emission line ratios, which we will address in the following section. However, from the success of this model, we can, with some confidence, make several statements about the physical conditions in these regions. First, the dominant source of ionization and heating is photoionization from the continuum radiation emitted by the central source. The estimate of the intrinsic SED and luminosity of the central source by Pier et al. (1994) is approximately correct, including the reflection fraction. There is a range of density within the emission line gas, and some of the gas is dusty. And, finally, it is likely that the elemental abundances in these regions are not solar.

6. Model Discrepancies

As discussed in section 2., the data obtained with FOS are spatially resolved. This permitted us to adjust more parameters, in particular abundances, than we have in previous studies (cf Kraemer et al. 1998). The result of this flexibility is a better set of predicted line

ratios than can usually be achieved with photoionization models, but there are still obvious discrepancies. These both show the limitations of these simple models and can be used to obtain additional physical insight. Although there are some weak lines which were not well fit by the models (e.g. [Mg V] λ 2929 and [Ne V] λ 2974), the fluxes of the weakest lines were difficult to measure accurately. We will, therefore, concentrate on the discrepancies in the predicted strengths of the stronger lines.

There are three high ionization UV lines for which the model predictions are most obviously discrepant: N IV] λ 1485, O III] λ 1664 and [Ne IV] λ 2424. The former two are predicted too strong, by factors of 4 and 3 respectively. The [Ne IV] line is predicted too weak by a factor of 4. The N IV] line is a strong coolant in both of the directly ionized components of the model. If the high ionization component was truncated at lower optical depth or was characterized by a higher ionization parameter, the N^{+3} zone would be smaller, reducing the strength of the λ 1485 line. This would also help reduce the relative strength of the O III] λ 1664 line. The problem is that it would worsen the fit for the [Ne V] and [Fe VII] lines. The weakness of the predicted [Ne IV] strength presents a different problem. With the SED assumed for these models, it takes a unique set of conditions to get a component in which the relative [Ne IV] strength is comparable to that observed. The contribution from such a component would be diluted by the other component spectra, still resulting in a relatively weak λ 2424 line. One possible explanation is that the electron temperatures predicted by these models is too low. A higher electron temperature in the O^{++} component would increase the strengths of the collisionally excited lines. Combined with the more highly ionized, high ionization component, the overall strength of the [Fe VII] and [Ne V] lines could be maintained, and [Ne IV] increased, while dropping the overall the N IV] and O III]. Although at first glance this might present a problem for the [O III] λ 5007/ λ 4363 ratio, the increase in the relative 4363 strength could be offset by lowering the density of the O^{++} component. The question is: what is the source of this additional

heating? We shall return to this question in the following section.

There are also discrepancies in the low excitation lines, which arise primarily in the shielded component. The most obvious problem is that the reddening corrected Balmer decrement is much steeper than predicted by the models, although this is biased somewhat in the average of the observations by the extremely high $N\alpha/H\beta$ ratio seen in the Position 3 spectrum. The predicted neutral oxygen lines are too strong, and the model predicts fairly strong [N I] emission, which we did not detect in the spectra. The Mg II $\lambda 2800$ line is too weak by approximately a factor of 3. Finally, either the emissivity or size of the partially ionized zone in the shielded component is insufficient. If more ionizing energy were injected into this gas, all of these discrepancies would be mitigated. A larger ionization fraction would drop the relative strength of the neutral lines. Increased heating and ionization would increase the emissivity of the gas. And, if the energy injection were in the form of energetic particles or increased X-ray ionization, enhanced collisional excitation of neutral hydrogen would increase the ratio of $H\alpha/H\beta$.

7. Discussion

Although photoionization by the central source is the dominant mechanism determining the physical conditions in these four regions, these simple models do not give the full picture of the underlying physics in the emission line gas. There appears to be additional heating and/or ionization from some source other than the assumed ionizing continuum.

There is evidence that emission line ratios in these regions are affected by processes other than pure photoionization. Kriss et al. (1992) have remarked on the surprising strength of the N III $\lambda 990$ and C III $\lambda 977$ resonance lines seen in HUT spectra of NGC 1068. Although these lines are outside the FOS bandpass, our model predictions of their

strengths relative to the intercombination lines, N III] $\lambda 1785$ and C III] $\lambda 1909$, are well below those measured in the HUT data (although we note that the HUT data area sampling a much larger region). Kriss et al. found similar problems with the model predictions for these lines and attributed their relative enhancement as due to additional heating of the emission line gas by shocks. Ferguson et al. (1995) have suggested that the enhancement is not due to shock heating but, rather, continuum fluorescence. Once a driver line is excited by absorption of a continuum photon, it will scatter and degrade into subordinate lines, resulting in enhancement of the resonance lines similar to that seen for the Lyman transitions in the Case B approximation for hydrogen (Osterbrock 1989). This process is only important for optically thick driver lines and is dependent on the line width and, therefore, the turbulent velocity in the emission line gas. Although it is likely that the conditions within the line formation regions are favorable for this process, it is difficult to determine how much enhancement there will be. For example, Ferguson et al. get only about half the observed value for Doppler widths ~ 1000 km/sec. Furthermore, the strengths of lines unaffected by continuum fluorescence are also underpredicted by the models. Therefore, it is likely that some type of additional heating is required.

Lame & Ferland (1991) have examined the relative contributions of photoionization and shocks to the excitation of the emission line gas in the planetary nebula NGC 6302. Their models of gas photoionization by a central star of temperature 450,000K accurately reproduced the relative strengths of most nebular lines, they could not match the observed strengths of the highest ionization lines, such as N IV] $\lambda 1485$, N V $\lambda 1240$, C IV $\lambda 1549$, [Ne IV] $\lambda 2424$, and [Ne V] $\lambda 3426$. Their conclusion was that the physical conditions in the nebula were likely to be the result of photoionization combined with collisional excitation from shocks due to stellar winds. It seems, at first, that such a combination of effects could resolve some of the discrepancies seen with our simple photoionization models.

If the additional heating is due to shocks, Kriss et al. (1992) suggest as one possible mechanism the interaction of the radio plasma ejected from the nucleus with the NLR clouds. This was first proposed by Wilson & Ulvestad (1983) after VLA maps of the radio emission in NGC 1068 revealed the existence of a jet within the NLR. The coincidence of the brightest [O III] knots with the radio bright spots (Evans et al. 1991) and recent FOC spectra showing possible jet driven motions in the NLR (Axon et al. 1998) support this scenario. As shown in Figure 1, the four regions discussed here all lie on or near the axis of the radio source, with Position 3 lying directly in its projected path. Although Position 3 is probably furthest from the ionizing source, its spectrum not only has the strongest high excitation lines (which may only be indicative of a greater fraction of optically thin gas), but the smallest [O III] $\lambda 5007/\lambda 4363$, indicating the highest electron temperature in the O⁺⁺ zone (assuming density similar to the other regions).

It then seems plausible that the additional heating we infer from our models may be the result of the result of a cloud/jet interaction. Is it less certain that the additional energy is the result of shock heating. Although it is likely that an additional heating source is present in the most highly ionized gas in these regions, it is also apparent from the model discrepancies that additional heating and ionization are required in the shielded gas. Ferland & Mushotzky (1984) have discussed the effects of the injection of relativistic electrons into emission-line gas for conditions applicable to the NLR of AGN. Their models predict an increase in the temperature, ionization fraction, and physical size of partially ionized or neutral gas deep within a photoionized emission line cloud, as well as the temperature and ionization fraction of the illuminated face of the cloud. In their simple model, relativistic electrons were able to penetrate up to column densities in excess of 10^{22}cm^{-2} , similar to the sizes of our model components. The plausibility of this explanation is supported by the fact that there is clearly a source for such energetic particles in the inner NLR, i.e. the radio jet, and that the spectrum of Position 3 shows the largest H α /H β ratio.

8. Conclusions

We have analyzed UV and optical spectra of the Seyfert 2 galaxy NGC 1068, obtained with the FOS on *HST*, from four regions within the inner NLR. Although these data were taken before the installation of COSTAR, we were able to determine that the contamination from the aberrated PSF did not significantly degrade the quality of the data obtained from two of the four pointings, providing us with three relatively distinct regions. We have constructed photoionization models to match an averaged set of conditions from these regions. The predicted emission line ratios fit the dereddened observed ratios for the large majority of emission lines, with the few exceptions noted in section 6. We were able to fit both permitted and forbidden lines and lines from a wide range of ionization state, e.g. N V as well as [N II], using a three-component model and a limited set of free parameters. Since these models are constrained by the best estimate of the underlying SED of the ionizing continuum and spatial information provided by the FOS data, we are confident that the general physical characteristics assumed in these models reflect the actual physical conditions in the NLR gas.

From our analysis and modeling of the spectra we can make several statements regarding the physical conditions in the inner NLR of NGC 1068. First of all, the dominant mechanism for ionizing the NLR gas is photoionization by continuum radiation from the central source. The estimates by Pier et al. (1994) and Miller et al. (1991) regarding the SED and intrinsic luminosity of the ionizing continuum are approximately correct. As noted by Netzer (1997) and Netzer & Turner (1997), the abundances in the emission line gas are not solar, although we found that enhancement of nitrogen was more likely than depletion of oxygen. Also, our models support Netzer’s suggestion that these regions include a mixture of dusty and dust-free gas.

There are two aspects of these models that provide us with additional insight into

the physical conditions in the NLR. First, as we discussed in detail in the previous two sections, the electron temperatures and, perhaps, ionization states predicted by the models are too low, although this is masked somewhat by our choice of initial conditions such as density. The most likely explanation, given the constraints on the SED, is that there is additional collisional heating and ionization. Kriss et al. (1992) have suggested that shock heating is an important process. Since additional heating and ionization are also needed in the partially ionized component, it may be that cosmic rays, perhaps associated with the radio jet, are the main source of additional energy. As shown by Ferland & Mushotzky (1984), relativistic electrons can penetrate through large column densities of atomic gas, affecting the extended partially ionized envelope. The location of the four regions in our data set with respect to the radio jet, particularly Position 3, supports the suggestion of a jet/cloud interaction, whether the additional heating is due to shocks, cosmic rays, or some combination of the two.

The other interesting aspect of the model is that the most likely source of the low ionization emission lines is gas that is partially screened by an optically thin component, probably of higher density. In fact, if there is additional heating beyond that due to photoionization, the ratio of the densities of the screening component to the low ionization gas may be even greater than assumed here (2:1). We would suggest that this density gradient is the result of material being swept up by the force of the jet, creating a thin wall of denser material nearest the ionizing source. This is in general agreement with the recent observations by Axon et al. (1998), which indicate that the gas with the strongest line emission lies along the direction of the radio jet, although this may be due, in part, to the collimation of the ionizing radiation.

Planned GTO and GO observations of NGC 1068 with the Space Telescope Imaging Spectrograph (STIS), on *HST*, will provide optical and UV spectra data with improved

spatial resolution over a larger section of the NLR. Better spatial resolution will permit us to examine conditions within these regions and may reveal more about their apparent inhomogeneity. From these data we can further examine the possibility of interaction between the radio jet and the ionized gas, including looking off the radio axis for NLR gas that may be unaffected by the jet. Such observations will go further in constraining the physical conditions and energy budget in the NLR.

REFERENCES

- Antonucci, R.R., & Miller, J.S. 1985, *ApJ*, 297, 621
- Antonucci, R.R. 1994, *ARA&A*, 31, 64
- Antonucci, R.R., Hurt, T., & Miller, J.S. 1994, *ApJ*, 430, 210
- Axon, D.J., et al. 1998, *ApJ*, in press
- Balick, B., & Heckman 1985, *AJ*, 90, 197
- Bergeron, J., Petitjean, P., & Durret, F. 1989, *Å*, 248, 127
- Bruhweiler, F.C., Truong, K.Q., & Altner, B. 1991, *ApJ*, 379, 596
- Caganoff, S., et al. 1991, *ApJ*, 377, L9
- Crenshaw, D.M., & Peterson, B.M. 1986, *PASP*, 98, 185
- Evans, I.N., & Dopita 1988, *ApJ*, 310, L15
- Evans, I.N. 1993, FOS Instrument Science Report, CAL/FOS-104, 1
- Ferguson, J.W., Ferland, G.J., & Pradhan, A.K. 1991, *ApJ*, 438, L55
- Ferland, G.J., & Mushotzky R.F. 1982, *ApJ*, 262, 564
- Ferland, G.J., & Mushotzky, R.F. 1984, *ApJ*, 286, 42
- Ferland, G.J., et al. 1996, *ApJ*, 461, 683
- Koski, A.T., 1978, *ApJ*, 223, 56
- Kraemer, S.B. 1985, Ph.D. thesis, Univ. Maryland
- Kraemer, S.B., & Harrington, J.P. 1986, *ApJ*, 307, 478
- Kraemer, S.B., Wu, C.-C., Crenshaw, D.M., & Harrington, J.P. 1994, *ApJ*, 435, 171
- Kraemer, S.B., Crenshaw, D.M., Filippenko, A.V. & Peterson, B.M. 1998, *ApJ*, in press
- Kriss, G.A., et al. 1992, *ApJ*, 394, L37

- Lame, N.J., & Ferland, G.J. 1991, *ApJ*, 367, 208
- Miller, J.S., & Antonucci, R.R 1983, *ApJ*, 271, L7
- Miller, J.S., Goodrich, R.W., & Mathews, W.G. 1991, *ApJ*, 378, 47
- Netzer, H. 1997, *Ap&SS*, 248, 127
- Netzer, H., & Turner, T.J. 1997, *ApJ*, 488, 694
- Oliva, E. 1997, in *Emission Lines in Active Galaxies: New Methods and Techniques*, ed. B.M. Peterson, F.-Z. Cheng, & A.S. Wilson (San Francisco: Astronomical Society of the Pacific), ASP Conference Series, 113, 288
- Osterbrock, D.E. 1974, *Astrophysics of Gaseous Nebulae* (San Francisco: W. H. Freeman)
- Osterbrock, D.E. 1989, *Astrophysics of Gaseous Nebulae and Active Galactic Nuclei* (Mill Valley, Univ. Science Books)
- Osterbrock, D.E. 1993, *ApJ*, 404, 551
- Pier, E.A., et al. 1994, *ApJ*, 428, 124
- Savage, B.D., & Mathis, J.S. 1979, *ARA&A*, 17, 73
- Seab, C.G., & Shull, J.M. 1983, *ApJ*, 275, 652
- Seaton, M.J. 1978, *MNRAS*, 185, 5P
- Seyfert, C.K. 1943, *ApJ*, 97, 28
- Snijders, M.A.J., Briggs, S.A., & Boksenberg, A. 1982, in *Proc. of 3rd European IUE Conf.*, ed. M. Grewing(ESA SP-176), 551
- Wilson, A.S., & Ulvestad, J.S. 1983, *ApJ*, 275, 8

Fig. 1.— FOC [O III] image of NGC 1068 with the four FOS aperture positions. The square pattern of spots with low counts are instrumental reseau marks. North is up and east is to the left. The apertures are $0''.3$ in diameter.

Fig. 2.— FOS Far-UV (G130H) spectra of NGC 1068 for the nucleus (“N”) and positions 1, 2, and 3).

Fig. 3.— FOS Near-UV (G190H, G270H) spectra of NGC 1068 for the nucleus (“N”) and positions 1, 2, and 3).

Fig. 4.— FOS Optical (G400H, G570H) spectra of NGC 1068 for the nucleus (“N”) and positions 1, 2, and 3).

Fig. 5.— Comparison of incident ionizing flux spectrum at the illuminated face of a directly photoionized cloud to the filtered flux spectrum used for the shielded model component.

Table 1. Log of FOS observations (0".3 diameter aperture)

Archive Name	Dataset Name	Detector	Grating	Exposure (sec)	Observation Date
NGC1068-NUC	Y0GQ0107T	FOS/BL	G130H	1500	1991 January 27
NGC1068-NUC	Y0GQ0106T	FOS/BL	G190H	1000	1991 January 27
NGC1068-NUC	Y0GQ0108T	FOS/BL	G270H	700	1991 January 27
NGC1068	Y0MW0707T	FOS/BL	G130H	1500	1991 June 25
NGC1068	Y0MW0706T	FOS/BL	G190H	1000	1991 June 25
NGC1068	Y0MW0806T	FOS/RD	G270H	700	1991 June 25
NGC1068	Y0MW0809T	FOS/RD	G400H	600	1991 June 25
NGC1068	Y0MW0807T	FOS/RD	G570H	600	1991 June 25
NGC1068-CLOUD1	Y0MW070AT	FOS/BL	G130H	1500	1991 June 25
NGC1068-CLOUD1	Y0MW0709T	FOS/BL	G190H	1000	1991 June 25
NGC1068-CLOUD1	Y0MW080BT	FOS/RD	G270H	700	1991 June 25
NGC1068-CLOUD1	Y0MW080ET	FOS/RD	G400H	600	1991 June 26
NGC1068-CLOUD1	Y0MW080CT	FOS/RD	G570H	600	1991 June 26
NGC1068-CLOUD2	Y0MW070DT	FOS/BL	G130H	1500	1991 June 25
NGC1068-CLOUD2	Y0MW070CT	FOS/BL	G190H	1000	1991 June 25
NGC1068-CLOUD2	Y0MW080GT	FOS/RD	G270H	700	1991 June 26
NGC1068-CLOUD2	Y0MW080JT	FOS/RD	G400H	600	1991 June 26
NGC1068-CLOUD2	Y0MW080HT	FOS/RD	G570H	600	1991 June 26
NGC1068-CLOUD3	Y19G0206T	FOS/BL	G130H	2000	1993 March 4
NGC1068-CLOUD3	Y19G0205T	FOS/BL	G190H	1350	1993 March 3
NGC1068-CLOUD3	Y19G0107T	FOS/RD	G270H	1000	1993 March 1
NGC1068-CLOUD3	Y19G0106T	FOS/RD	G400H	850	1993 March 1
NGC1068-CLOUD3	Y19G0105T	FOS/RD	G570H	850	1993 March 1

Table 2. Dereddened Line ratios from FOS positions (relative to $H\beta$)

	Nucleus	Position 1	Position 2	Position 3
$Ly\alpha$ $\lambda 1216$	11.83 (± 1.11)	18.91 (± 2.68)	12.03 (± 2.88)	16.66 (± 3.95)
N V $\lambda 1240$	4.86 (± 0.38)	10.74 (± 1.72)	7.87 (± 1.65)	8.78 (± 2.52)
Si IV $\lambda 1398$ / O IV] $\lambda 1402$	1.30 (± 0.22)	2.09 (± 0.47)	2.38 (± 0.57)	1.55 (± 0.62)
N IV] $\lambda 1486$	0.47 (± 0.15)	1.39 (± 0.31)	1.80 (± 0.43)	1.65 (± 0.31)
C IV $\lambda 1550$	6.93 (± 0.23)	9.72 (± 0.96)	8.65 (± 1.07)	9.60 (± 1.60)
He II $\lambda 1640$	3.20 (± 0.24)	3.05 (± 0.35)	3.06 (± 0.43)	4.26 (± 0.73)
O III] $\lambda 1663$	0.36 (± 0.10)	0.28 (± 0.16)	0.22 (± 0.13)	0.61 (± 0.11)
$\lambda 1718?$	—	0.44 (± 0.16)	0.36 (± 0.18)	1.17 (± 0.19)
N III] $\lambda 1750$	0.38 (± 0.05)	0.48 (± 0.15)	0.67 (± 0.34)	0.81 (± 0.23)
$\lambda 1804?$	0.21 (± 0.05)	0.55 (± 0.18)	0.67 (± 0.36)	0.80 (± 0.29)
C III] $\lambda 1909$, Si III] $\lambda 1892$	3.99 (± 0.25)	3.80 (± 0.41)	4.78 (± 0.52)	5.04 (± 1.01)
$\lambda 2143?$	0.23 (± 0.02)	0.44 (± 0.12)	0.72 (± 0.21)	0.68 (± 0.30)
[O III] $\lambda 2321$ /C II] $\lambda 2326$	1.51 (± 0.15)	1.18 (± 0.18)	0.91 (± 0.14)	0.88 (± 0.24)
[Ne IV] $\lambda 2423$	1.97 (± 0.21)	1.72 (± 0.17)	1.66 (± 0.18)	3.25 (± 0.54)
[O II] $\lambda 2470$	0.27 (± 0.07)	0.20 (± 0.04)	0.17 (± 0.04)	0.37 (± 0.14)
He II $\lambda 2512$	0.27 (± 0.05)	0.22 (± 0.04)	0.14 (± 0.04)	0.22 (± 0.05)
$\lambda 2628?$	0.49 (± 0.05)	0.55 (± 0.06)	0.23 (± 0.08)	0.31 (± 0.08)
He II $\lambda 2734$	0.37 (± 0.03)	0.28 (± 0.06)	0.16 (± 0.06)	0.24 (± 0.03)
Mg II $\lambda 2800$	1.97 (± 0.10)	1.28 (± 0.18)	1.01 (± 0.10)	1.11 (± 0.11)
[Mg V] $\lambda 2929$	0.21 (± 0.02)	0.22 (± 0.04)	0.11 (± 0.02)	0.08 (± 0.02)
[Ne V] $\lambda 2974$	0.28 (± 0.05)	0.25 (± 0.03)	0.14 (± 0.03)	0.12 (± 0.03)
$\lambda 3045?$	0.29 (± 0.06)	0.27 (± 0.07)	0.15 (± 0.06)	0.17 (± 0.08)
O III $\lambda 3133$	0.95 (± 0.02)	0.66 (± 0.04)	0.56 (± 0.04)	0.63 (± 0.12)
He II $\lambda 3204$	0.27 (± 0.04)	0.29 (± 0.05)	0.25 (± 0.04)	0.36 (± 0.04)
[Ne V] $\lambda 3346$	0.81 (± 0.02)	1.29 (± 0.05)	1.02 (± 0.04)	1.66 (± 0.10)
[Ne V] $\lambda 3426$	2.32 (± 0.05)	3.45 (± 0.11)	2.67 (± 0.09)	4.29 (± 0.22)

Table 2—Continued

	Nucleus	Position 1	Position 2	Position 3
[Fe VII] λ 3588	0.19 (\pm 0.03)	0.15 (\pm 0.02)	0.17 (\pm 0.03)	0.20 (\pm 0.03)
[O II] λ 3727	0.46 (\pm 0.02)	0.55 (\pm 0.05)	0.83 (\pm 0.04)	1.25 (\pm 0.06)
[Fe VII] λ 3760	0.37 (\pm 0.02)	0.26 (\pm 0.04)	0.18 (\pm 0.03)	0.32 (\pm 0.02)
[Ne III] λ 3869	2.46 (\pm 0.13)	2.41 (\pm 0.08)	2.02 (\pm 0.10)	2.51 (\pm 0.09)
[Ne III] λ 3967	0.72 (\pm 0.04)	0.85 (\pm 0.02)	0.81 (\pm 0.06)	0.91 (\pm 0.06)
[S II] λ 4072	0.28 (\pm 0.03)	0.31 (\pm 0.01)	0.35 (\pm 0.03)	0.30 (\pm 0.18)
H δ λ 4100	0.30 (\pm 0.03)	0.32 (\pm 0.02)	0.30 (\pm 0.05)	0.32 (\pm 0.02)
H γ λ 4340	0.47 (\pm 0.01)	0.56 (\pm 0.03)	0.53 (\pm 0.03)	0.53 (\pm 0.06)
[O III] λ 4363	0.51 (\pm 0.04)	0.45 (\pm 0.03)	0.34 (\pm 0.07)	0.54 (\pm 0.08)
He II λ 4686	0.44 (\pm 0.03)	0.42 (\pm 0.01)	0.42 (\pm 0.03)	0.59 (\pm 0.06)
H β	1.00	1.00	1.00	1.00
[O III] λ 5007	13.14 (\pm 0.07)	14.85 (\pm 0.19)	15.40 (\pm 0.21)	17.11 (\pm 0.14)
[Fe VII] λ 5721	0.48 (\pm 0.11)	0.37 (\pm 0.04)	0.25 (\pm 0.03)	0.38 (\pm 0.03)
He I λ 5876	0.13 (\pm 0.01)	0.14 (\pm 0.02)	0.27 (\pm 0.04)	0.17 (\pm 0.04)
[Fe VII] λ 6087	0.71 (\pm 0.09)	0.48 (\pm 0.03)	0.27 (\pm 0.02)	0.47 (\pm 0.05)
[O I] λ 6300	0.41 (\pm 0.04)	0.50 (\pm 0.02)	0.42 (\pm 0.03)	0.47 (\pm 0.03)
[O I] λ 6364/[Fe X] λ 6374	0.37 (\pm 0.15)	0.31 (\pm 0.03)	0.12 (\pm 0.02)	0.20 (\pm 0.02)
[N II] λ 6548, 6584	4.45 (\pm 0.62)	4.86 (\pm 0.34)	4.81 (\pm 0.84)	5.14 (\pm 0.33)
H α λ 6563	4.07 (\pm 0.11)	4.87 (\pm 0.49)	5.19 (\pm 0.49)	6.24 (\pm 0.64)
[S II] λ 6716, 6731	0.39 (\pm 0.05)	0.42 (\pm 0.03)	0.55 (\pm 0.03)	0.71 (\pm 0.05)
Flux (H β) ^a	1.65 x 10 ⁻¹³	1.26 x 10 ⁻¹³	9.20 x 10 ⁻¹⁴	5.61 x 10 ⁻¹⁴
E(B-V)	0.02 (\pm 0.01)	0.22 (\pm 0.02)	0.20 (\pm 0.03)	0.24 (\pm 0.04)

^aergs s⁻¹ cm⁻²

Table 3. Line Ratios from Model Components and Best Fit Composite (relative to $H\beta$)

	High Ionization ^a	O ^{++b}	Shielded ^c	Composite ^d	Average Observed ^e
C III λ 977	0.41	0.17	0.11	0.22	
N III λ 990	0.17	0.20	0.05	0.16	
O VI λ 1036	12.81	1.63	0.00	4.01	
OV λ 1216	8.26	2.08	0.01	3.11	
Ly α λ 1216	33.54	4.55	27.59	17.56	14.69
N V λ 1240	22.04	1.48	0.02	6.25	8.15
Si IV λ 1398	0.03	0.02	0.17	0.05	incl w/ O IV]
O IV] λ 1402	4.53	2.39	0.01	2.33	1.88
N IV] λ 1486	7.65	5.26	0.46	4.63	1.46
C IV λ 1550	28.12	1.67	1.38	8.21	8.86
He II λ 1640	7.62	3.83	0.21	3.85	3.48
O III] λ 1663	0.55	1.16	0.97	0.95	0.38
N III] λ 1750	0.66	1.58	1.14	1.23	0.64
Si III] λ 1892	0.00	0.06	0.42	0.14	incl w/ C III]
C III] λ 1909,	1.99	1.82	3.76	2.34	4.57
O III] λ 2321	0.04	0.09	0.12	0.09	incl w/ C II]
C II] λ 2326	0.00	0.02	2.17	0.55	1.05
[Ne IV] λ 2423	0.42	0.84	0.10	0.55	2.25
[O II] λ 2470	0.00	0.01	0.51	0.13	0.26
Mg II λ 2800	0.00	0.04	1.65	0.43	1.25
[Mg V] λ 2929	0.03	0.02	0.00	0.02	0.14
[Ne V] λ 2974	0.03	0.02	0.00	0.02	0.18
He II λ 3204	0.43	0.24	0.01	0.23	0.30
[Ne V] λ 3346	1.10	1.06	0.00	0.81	1.24
[Ne V] λ 3426	3.00	2.90	0.02	2.20	3.28
[Fe VII] λ 3588	0.23	0.15	0.00	0.13	0.18
[O II] λ 3727	0.00	0.02	2.16	0.54	0.86
[Fe VII] λ 3760	0.32	0.19	0.00	0.18	0.27

Table 3—Continued

	High Ionization ^a	O ^{++b}	Shielded ^c	Composite ^d	Average Observed ^e
[Ne III] λ 3869	0.01	1.94	6.81	2.65	2.32
[Ne III] λ 3967	0.00	0.60	2.11	0.83	0.84
[S II] λ 4072	0.00	0.00	0.48	0.12	0.32
H δ λ 4100	0.26	0.25	0.26	0.26	0.31
H γ λ 4340	0.47	0.46	0.47	0.47	0.53
[O III] λ 4363	0.18	0.67	0.55	0.51	0.45
He II λ 4686	1.03	0.59	0.03	0.56	0.48
H β	1.00	1.00	1.00	1.00	1.00
[O III] λ 5007	4.34	22.77	29.88	19.75	15.50
[N I] λ 5198, 5200	0.00	0.00	2.51	0.63	-
[Fe VII] λ 5721	0.37	0.26	0.01	0.22	0.35
He I λ 5876	0.00	0.06	0.12	0.06	0.16
[Fe VII] λ 6087	0.54	0.39	0.01	0.33	0.45
[O I] λ 6300	0.00	0.00	5.27	1.30	0.45
[O I] λ 6364	0.00	0.00	1.73	0.43	0.22
[Fe X] λ 6374	0.90	0.08	0.00	0.27	incl w/ [O I]
[N II] λ 6548, 6584	0.00	0.11	16.89	4.23	4.87
H α λ 6563	2.76	2.97	3.93	3.13	5.30
[S II] λ 6716, 6731	0.00	0.00	2.07	0.51	0.56

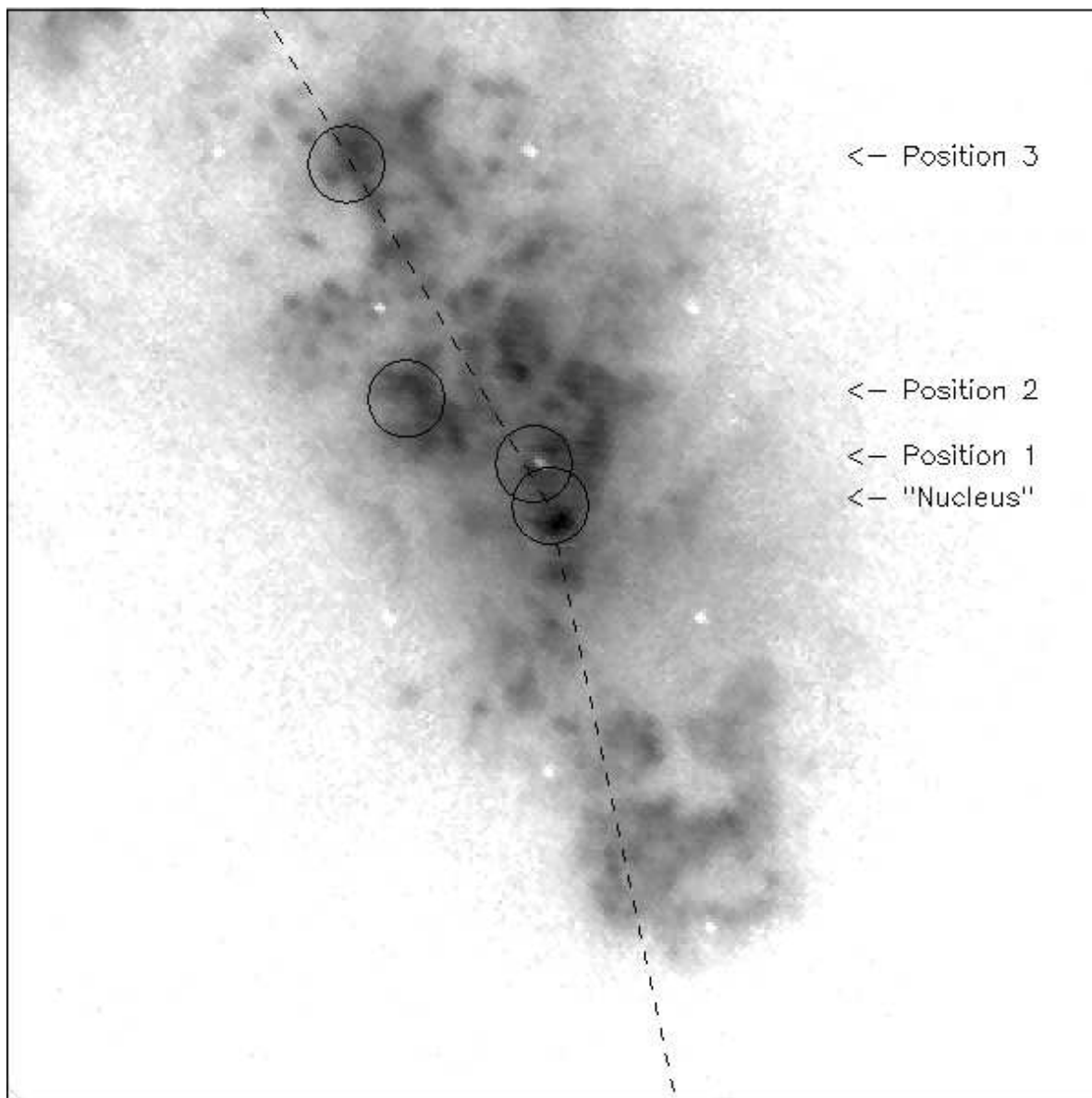
^aU = 10^{-1} , $N_H=5 \times 10^4$, no dust

^bU = $10^{-1.3}$, $N_H=1 \times 10^5$, 50% silicate dust, 75% graphite dust

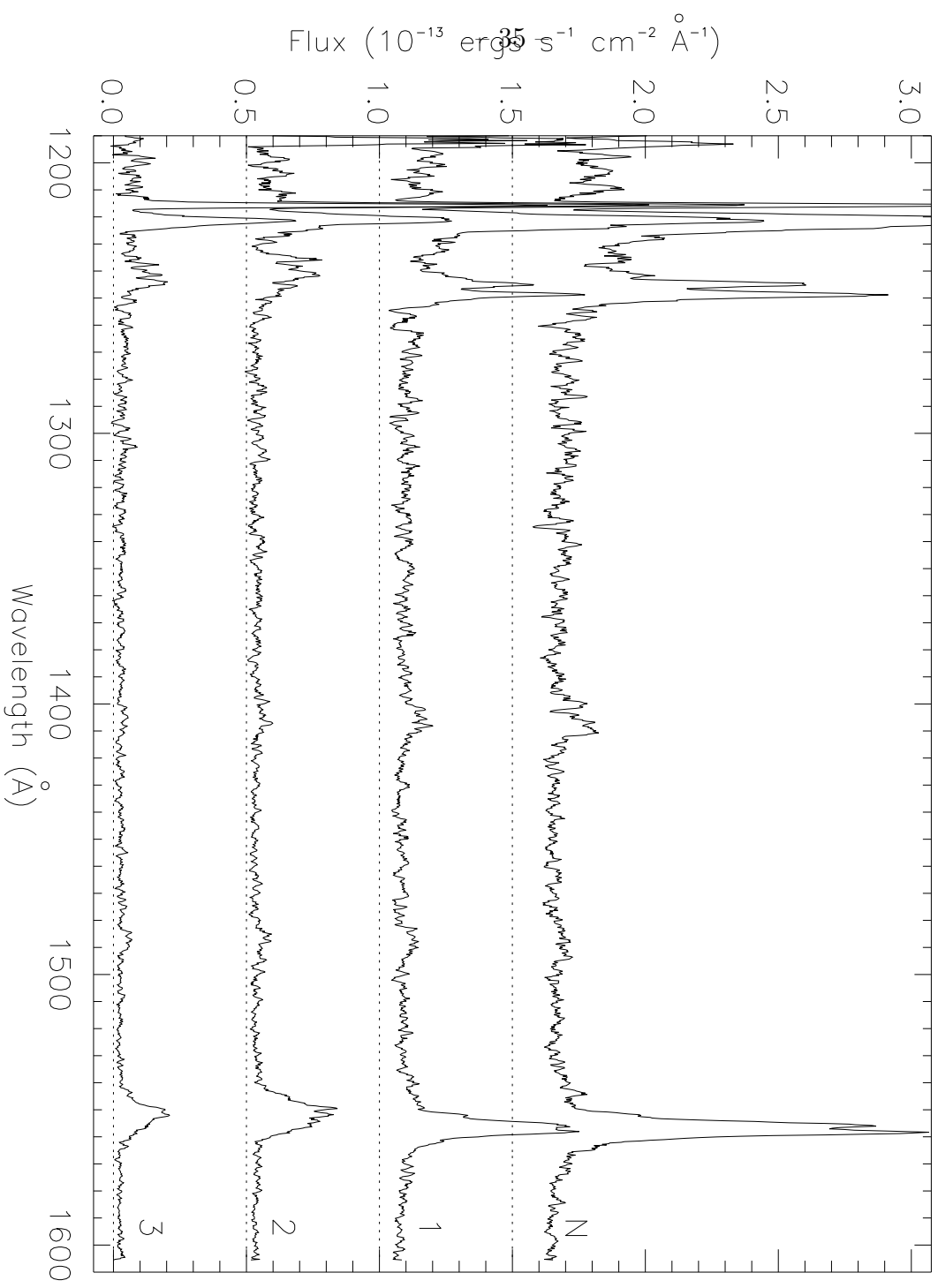
^cU = $10^{-2.35}$, $N_H=5 \times 10^4$, 30% graphite dust

^d25% from hi-ionization, 50% from O⁺⁺, 25% from shielded

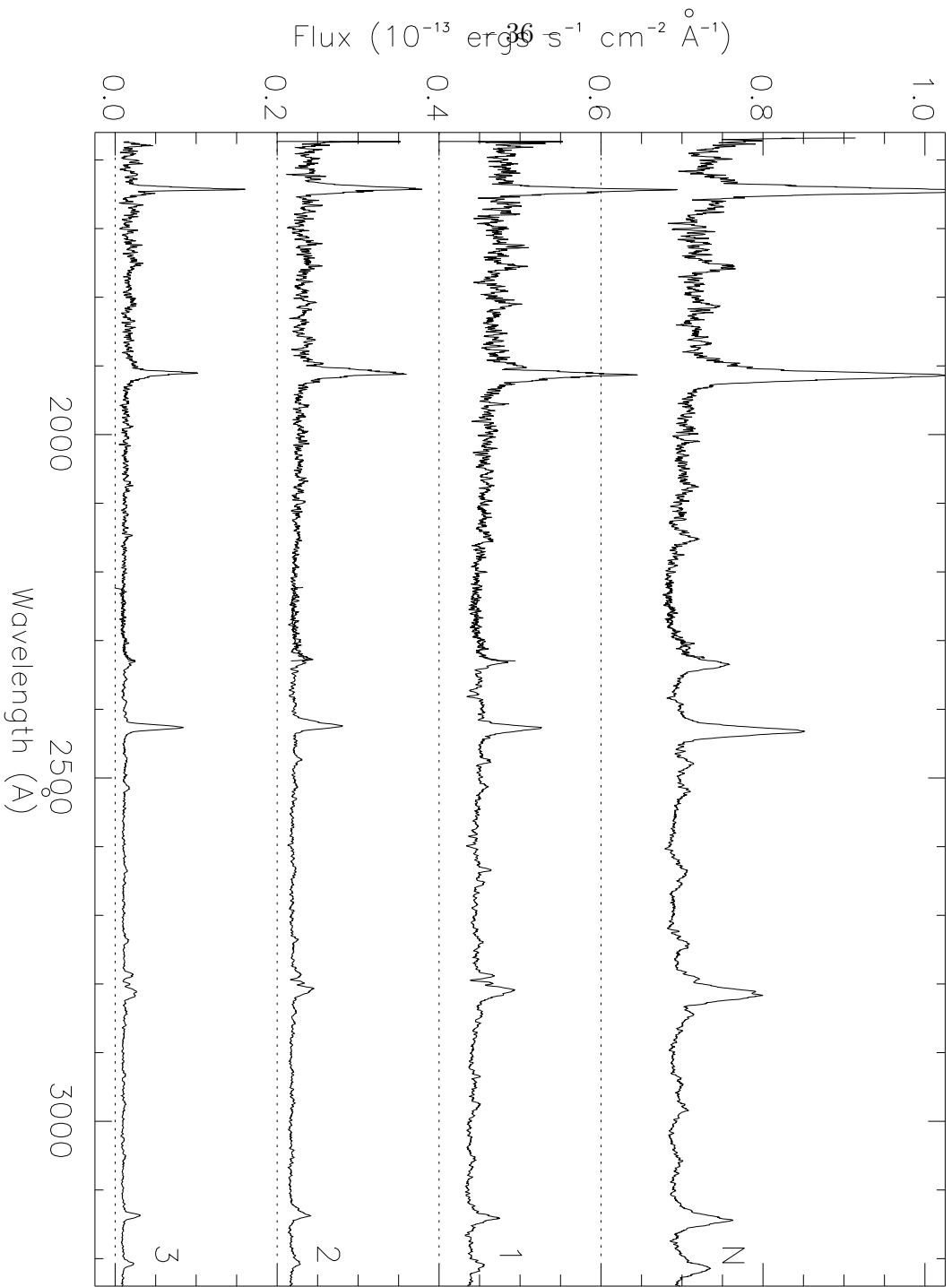
^eaverage = 12.5% each, Nucleus, Position 1; 25% each, Position 2, Position 3



NGC 1068 – FOS Far-UV Spectra



NGC 1068 – FOS Near-UV Spectra



NGC 1068 – FOS Optical Spectra

